The Astrophysical Journal, 648:732–740, 2006 September 1

CORONAL MAGNETIC FIELD TOPOLOGY OVER FILAMENT CHANNELS: IMPLICATION FOR CORONAL MASS EJECTION INITIATIONS

Yan Li and Janet Luhmann
Space Sciences Laboratory, University of California, Berkeley, CA 94720-7450; yanli@ssl.berkeley.edu, jgluhman@ssl.berkeley.edu
Received 2006 March 10; accepted 2006 May 4

ABSTRACT

The magnetic field topology at the coronal mass ejection (CME) source regions has been one of the major focuses of CME initiation models. While the "breakout" model requires a quadrupolar magnetic topology in the solar corona to enable an eruption, other models have shown that a bipolar magnetic topology can be the source region of a CME. In this paper, we use observational data and a potential field source surface model to investigate the magnetic field topology over CME productive quiescent filaments. A total of 80 quiescent filament–associated CME events during 1996–2004, spanning almost one solar cycle, with angular width $\geq 80^{\circ}$ are selected for this study. We found both bipolar topology and quadrupolar topology at CME source regions. This observational test of the assumptions of theoretical CME models suggests that bipolar topology is more common overall and in each year. The total occurrence ratio between quadrupolar and bipolar topology is about 1 : 3 with this selection of events. On the rising phase of the solar cycle, there is mostly bipolar topology, but on the declining phase, there is a mixture of both bipolar and quadrupolar topology. The bipolar topology occurrence has no clear solar cycle dependence. The quadrupolar topology occurrence peaks on the declining phase in the current solar cycle 23.

Subject headings: Sun: activity — Sun: coronal mass ejections (CMEs) — Sun: filaments — Sun: magnetic fields — Sun: prominences

Online material: color figures

1. INTRODUCTION

Despite tremendous progress in understanding coronal mass ejections (CMEs) in recent years, CME initiations are still a mystery (Forbes 2000; Moore & Sterling 2006). Debates among CME models are not conclusive (Linker & Mikic 1995; Antiochos 1998; Antiochos et al. 1999; Forbes 2000; Linker et al. 2001, 2003; Amari et al. 2003a, 2003b; Lynch et al. 2004; DeVore & Antiochos 2005; Gibson et al. 2004; Gibson & Fan 2006). The magnetic field topology at the CME source regions has been a major focus of CME initiation models. It is widely accepted in the community that CMEs are driven by magnetic free energy. Aly (1991) and Sturrock (1991) have shown that a fully open field for a given flux distribution has the maximum magnetic energy. It seems difficult for the eruption process to open the field lines and at the same time to release energy. The so-called breakout model (Antiochos 1998; Antiochos et al. 1999) solves this problem by requiring a multiflux system or a quadrupolar topology. When the sheared structure at the base rises due to certain mechanisms and pushes the lower field arcade up against the overlying upper field arcade, instead of opening the overlying field lines, the process transfers the upper closed field lines from one system to other systems (the side arcades) through magnetic reconnection between the large-scale overlying arcade and lower central arcade immediately over the sheared structure to let out the eruption. In order for the reconnection to take place, the overlying field arcade and the lower central field arcade need to have an antiparallel component. On the other hand, Linker et al. (2001, 2003) showed with MHD simulations that an adequate amount of flux cancellation at the magnetic neutral line at the base of a bipolar region may also lead to the eruption of a sheared structure and the overlying arcade. All closed-field arcades over the sheared structure are set in one direction, or parallel in their model. They pointed out that the flux cancellation decreases the "open field energy" of the system. In this paper, we also name the two topologies "antiparallel" and "parallel" topology, respectively, referring to the relationship between the erupting small arcade and the overlying large-scale arcade.

CMEs are gigantic ejected plasmoids from the Sun, often with organized magnetic structure, carrying masses typically 10^{15}–10^{16} g and total energy of 10^{30}–10^{31} ergs (Howard et al. 1985; Vourlidas et al. 2000). Evidently, CMEs are the most important space weather driver and are responsible for the most intense geomagnetic storms (Gosling et al. 1991; Gosling 1993; Webb 1995; St. Cyr et al. 2000; Li & Luhmann 2004). They may also play a role in the solar magnetic field evolution over the solar cycle by expelling magnetic fluxes (McComas et al. 1995; Low 1996; Luhmann et al. 1998; Gopalswamy et al. 2003b). CMEs take place frequently, on average from $\sim$0.5 per day at solar minimum to several per day around solar maximum (St. Cyr et al. 2000; Yashiro et al. 2004). The speed of CMEs ranges from <100 to >3000 km s^{-1}. There has not been any attempt to verify what kind of coronal magnetic topology is most responsible for spawning CMEs in reality. It is also interesting and important to find out whether the most energetic CMEs are associated with a certain topology. In this effort, we use observational data and a potential field source surface (PFSS) model to investigate the magnetic topology at the source regions of quiescent filament–associated CMEs. CMEs are found associated with active region flares as well as quiescent filaments or prominences (Bothmer & Schwenn 1994; Cliver et al. 1994; Webb 1998, 2000; Gilbert et al. 2000; Zhang et al. 2001; Li et al. 2001; Gopalswamy et al. 2003a, 2003b; Cremades & Bothmer 2004; Jing et al. 2004). The quiet region magnetic fields are generally less complex and so more readily analyzed for their topology. Their coronal fields are also the most likely to be well described with a potential field model apart from the central sheared structure that is not our particular concern for this study.

Starting around solar minimum, bipolar active regions emerge with the same leading polarity as the polar region field polarity in the same hemisphere. At about the solar maximum, the polar

fields reverse; therefore, during the declining phase, the active region leading polarities are in general opposite of the polar field in the same hemisphere. The active region fields will subsequently decay and be distorted by motions including differential rotation and meridional flow. With our selection of events spanning almost the entire solar cycle 23, we also study whether a particular magnetic topology is more important for initiating CMEs associated with quiescent filaments at different phases of the solar cycle.

2. EVENTS SELECTION

Our event selection began with the LASCO CME catalog complied by N. Gopalswamy & S. Yashiro (Yashiro et al. 2004).[1] Between 1996 and 2004, the total number of CMEs recorded in the catalog is 9239. For this study, CMEs with angular widths $\geq 80^\circ$ are considered, which reduces the number of CMEs of interest to 2209. We then use the *Solar and Heliospheric Observatory* (*SOHO*) EUV Imaging Telescope (EIT) 195 movies linked in the same catalog and Big Bear Solar Observatory (BBSO) Hα images and movies from the BBSO ftp archive[2] to select quiescent filament–related CMEs and identify the filament channels in the magnetic field using *SOHO* Michelson Doppler Imager (MDI) or Global Oscillation Network Group (GONG) magnetograms. Only those events with speed estimates and available EIT, BBSO Hα, and magnetogram observations are qualified for further selections. Finally, an event is selected when the correspondence between a LASCO CME and a quiescent filament disappearance can be positively identified and, at the same time, the filament channel can be confidently located in MDI (or GONG) magnetograms. Many events at the east limb cannot be selected for the study, because the filament channels cannot be located with confidence, while west-limb events can be selected when we can trace back a few days and identify the filament on the disk before the eruption. For our study a total of 99 events are selected from the 1996–2004 *SOHO* observations. With this group of events, Mount Wilson Observatory (MWO) synoptic maps and PFSS spherical harmonic coefficients are then used to extrapolate field lines over the filament channels and large-scale overlying field arcades. We calculate the large-scale closed arcades where the apex of the arcades reach the PFSS model source surface at 2.5 $R_\odot$, the upper boundary of the coronal helmet streamer belt. Filament channels of 67 events originating under these large-scale coronal streamer arcades are first selected. The filament channels of the other 32 events are not under the main coronal helmet streamer arcades. For these we calculated large-scale arcades at two lower heights with the apex at 2.0 and 1.5 $R_\odot$. Thirteen of the 32 events are found under the lower large-scale arcades canopy, giving a total of 80 events for which the relationship between the small-scale field at the filament channel and the large-scale overlying field can be studied. We therefore include the 80 events in this paper and eliminate 19 of our original events for this study. Most of the 19 eliminated events are from around the solar maximum period, when the streamer arcades are often complex and very warped, whereas near solar minimum the large-scale arcades encompass most of the solar globe except for the polar regions. The magnetic field topology at the source region and other characteristics of 80 of the 99 events are analyzed in this paper.

3. ANALYSES

In this section, we use a few examples to demonstrate our analyses. (For a list of all 80 events, see Table 1 in the Appendix.) The first case presented here is a halo CME on 1997 September 28.

[1] See http://cdaw.gsfc.nasa.gov/CME_list.
[2] See http://www.bbso.njit.edu.

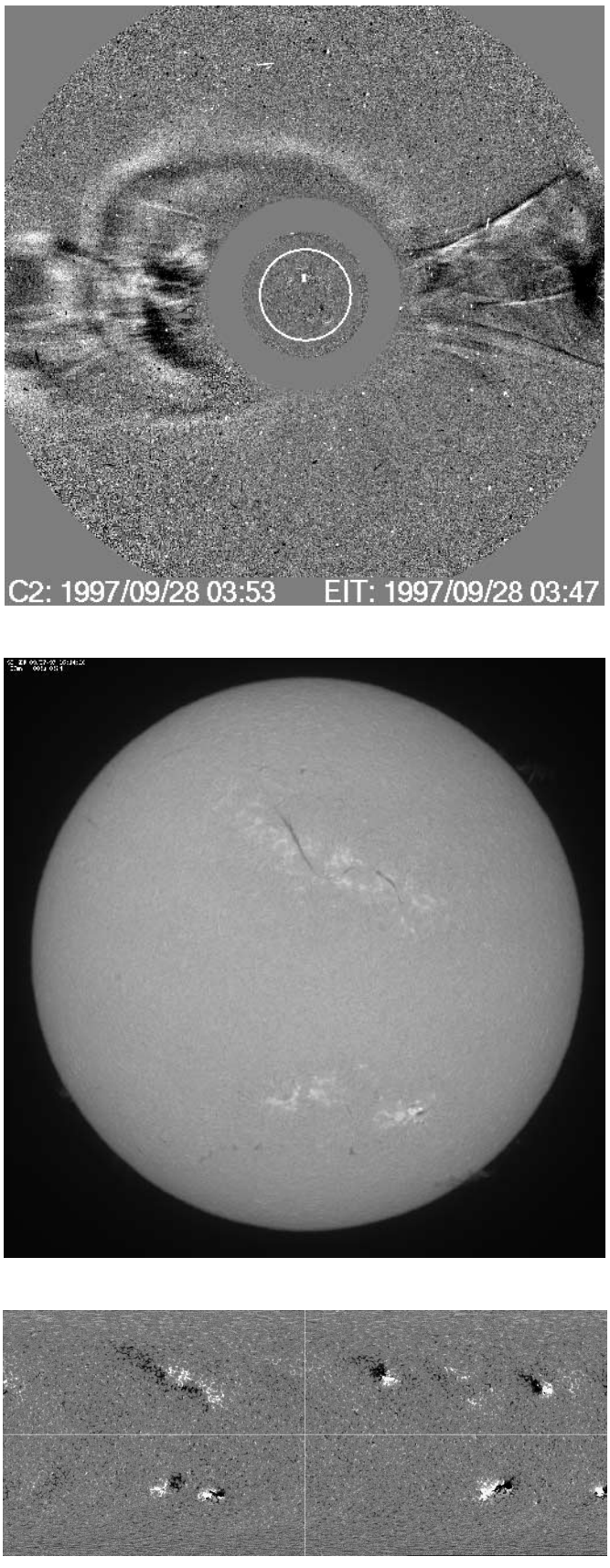

FIG. 1.—Halo CME on 1997 September 28. *Top*: LASCO C2 and EIT combined difference image. *Middle*: Long filament at the northern hemisphere near the central meridian on September 26 in the BBSO Hα image. *Bottom*: Elongated filament channel in magnetogram is shown with MDI synoptic map CR 1927 between Carrington longitude 60° and 120° and latitude 20° and 50° north (centered ~35° N). [*See the electronic edition of the Journal for a color version of this figure.*]

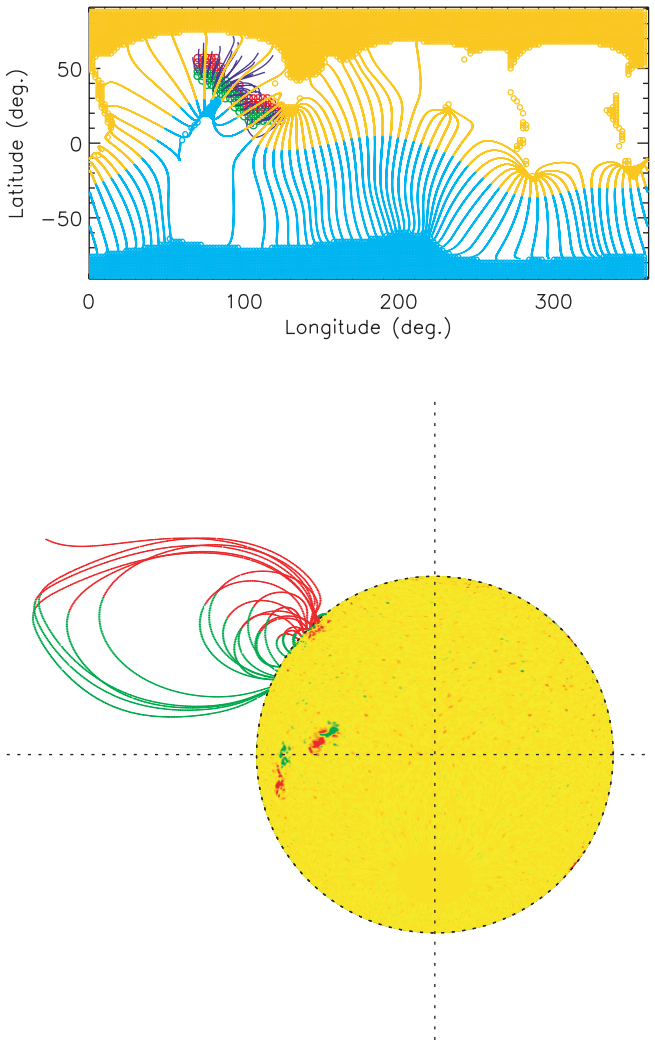

FIG. 2.—*Top*: PFSS model of field lines over the filament channel and large-scale field lines for 1997 September 28 CME. The filament channel is represented with the red and green patches for positive and negative magnetic field, respectively, and the blue field lines are those that have footpoints in these patches. Orange and aqua regions are positive and negative coronal holes, respectively. The orange and aqua field lines are the large-scale coronal streamer arcades; the orange portion indicates that the radial field component is pointing up and the aqua portion that the field is pointing down. *Bottom*: Spherical projection of field lines around CR longitude 75° and MDI synoptic map to further illustrate that the field lines over the filament and the large-scale field lines are parallel to each other, where the red portion of the field lines indicates that the radial field component is pointing up and the green portion that the field is pointing down. This region has parallel topology.

Figure 1 (*top*) shows a LASCO C2 and EIT combined difference image for this event. A long filament may be seen in the northern hemisphere near the central meridian on September 26 in the BBSO Hα image in Figure 1 (*middle*). The disappearance of this filament the end of the next day resulted in a halo CME at 01:08 UT on September 28 with a plane of sky speed of 359 km s^{-1} in the CME catalog. The elongated filament channel in the magnetogram is shown with a MDI synoptic map for Carrington rotation (CR) 1927 between Carrington longitude 60° and 120° and latitude 20° and 50° north (or centered about 35°N) in Figure 1 (*bottom*). Using MWO PFSS spherical harmonic coefficients (R. Ullrich & C. N. Arge 2004, private communication), we traced field lines from the filament channel and large-scale field lines of the helmet streamer belt shown in Figure 2 (*top*). The filament channel is represented with the red (positive magnetic field) and green (negative) patch, and the blue field lines are those that have footpoints in these patches. Orange and aqua regions represent positive and negative coronal holes, respectively. The orange and aqua field lines are the large-scale coronal streamer arcades; the orange portion of the field lines indicates that the radial field component is pointing up and the aqua portion indicates that the field is pointing down. In this case, the field lines immediately over the filament and the large-scale field lines are parallel to each other, which is further illustrated with a spherical projection in Figure 2 (*bottom*), where the red portion of the field lines indicates that the radial field component is pointing up and the green portion indicates the field is pointing down. This field topology is the same kind that was employed in the "flux cancellation" CME model of Linker et al. (2001, 2003), where no reconnection is possible between the lower coronal field arcades and the upper arcades. This is what we call a parallel topology.

The second case is a classic three-part limb CME (front, cavity, and core) from the northwest on 2003 February 18, seen in Figure 3 (*top*) with a LASCO and EIT combined image. A filament with more substantial thickness and length may be seen in the northern hemisphere and slightly to the west on February 17 in the BBSO Hα image in Figure 3 (*middle*). The disappearance of this filament the next day accompanied the limb CME at 02:42 UT with a plane of the sky speed of 888 km s^{-1} according to the CME catalog. The long and well-defined filament channel in the magnetogram is shown with the MDI synoptic map for CR 1999 between Carrington longitude 30° and 100° and centered about latitude 35°N in Figure 3 (*bottom*). Again, using MWO PFSS spherical harmonic coefficients, we traced field lines from the filament channel and large-scale field lines (see Fig. 4, *top*). As in the first example described above, the filament channel is represented with red (positive magnetic field) and green (negative) patches, and the blue field lines are those that have footpoints in these patches. Orange and aqua regions represent positive and negative coronal holes, respectively. The orange and aqua field lines are the large-scale coronal streamer arcades; the orange portion of the field lines indicates that the radial field component is pointing up and the aqua portion indicates that the field is pointing down. In this event, the field lines immediately over the filament and the outermost large-scale field lines are antiparallel to each other, which is further illustrated with a spherical projection in Figure 4 (*bottom*), where the red portion of the field lines indicates that the radial field component is pointing up and the green portion that the field is pointing down. The multiflux topology of the field lines closely resembles what the CME breakout model of Antiochos (1998, 1999) requires. There are four flux systems, the central small field arcade and two adjacent field arcades on each side, and a large-scale field arcade overhead. The central small arcade that overlies the erupting filament channel has a field direction that is antiparallel with the overlying large-scale arcade setting a favorable condition for reconnection between the two systems when the small arcade rises up against the overlying one. The mechanisms for the small arcade to rise is not restricted to any kind by the model. The structure may be destabilized by flux cancellation, flux emergence, or any other cause.

There are a few different terms used in the solar physics community and this paper in reference to these two different magnetic field topologies. These terms represent the same topology: "flux cancellation topology," "bipolar topology," "single arcade topology," and "parallel topology," and similarly these terms represent the other topology: "breakout topology," "quadrupolar topology," "multiflux system topology," and "antiparallel topology." Each of these terms emphasizes some aspects of the topology. For instance, as mentioned above, flux cancellation

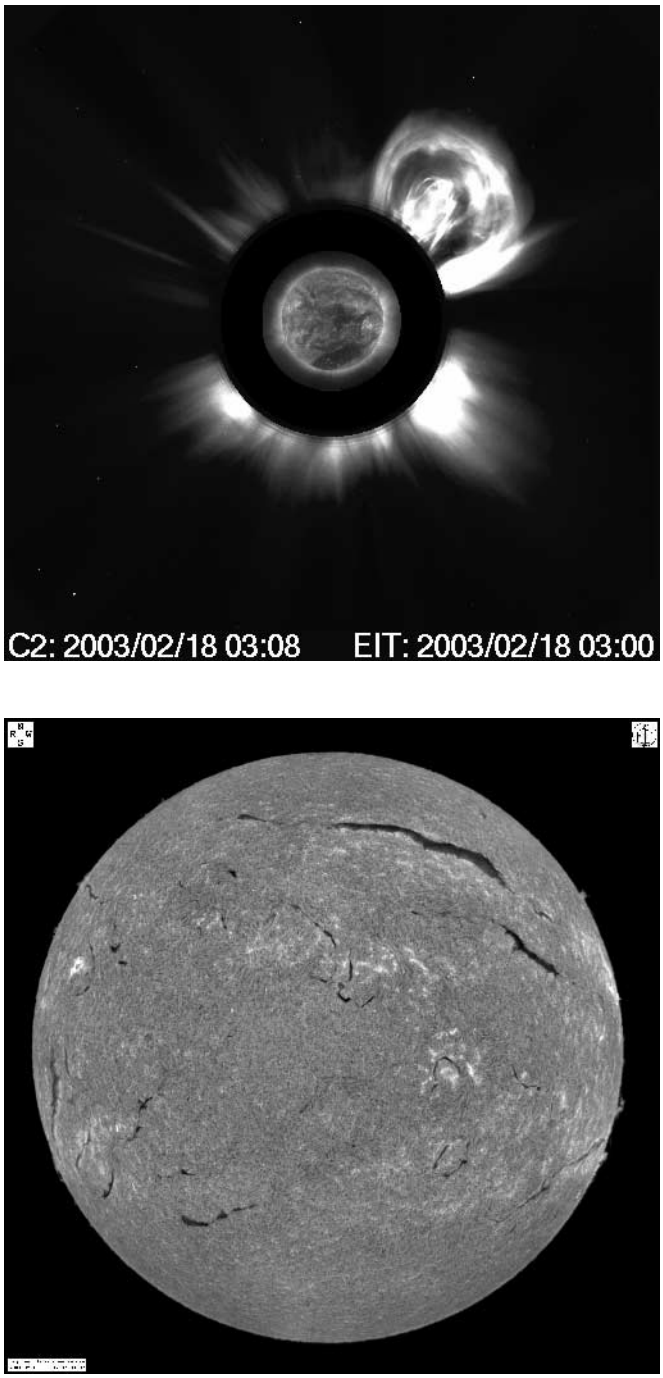

FIG. 3.—Classic three-part limb CME on 2003 February 18. *Top*: LASCO and EIT combined image. *Middle*: Filament with substantial thickness and length seen at the north on February 17 in the BBSO Hα image. *Bottom*: Long and well-defined filament channel in the magnetogram is shown with MDI synoptic map CR 1999 between Carrington longitude 30° and 100° and latitude 25° and 55° north (centered ~35° N). [*See the electronic edition of the Journal for a color version of this figure.*]

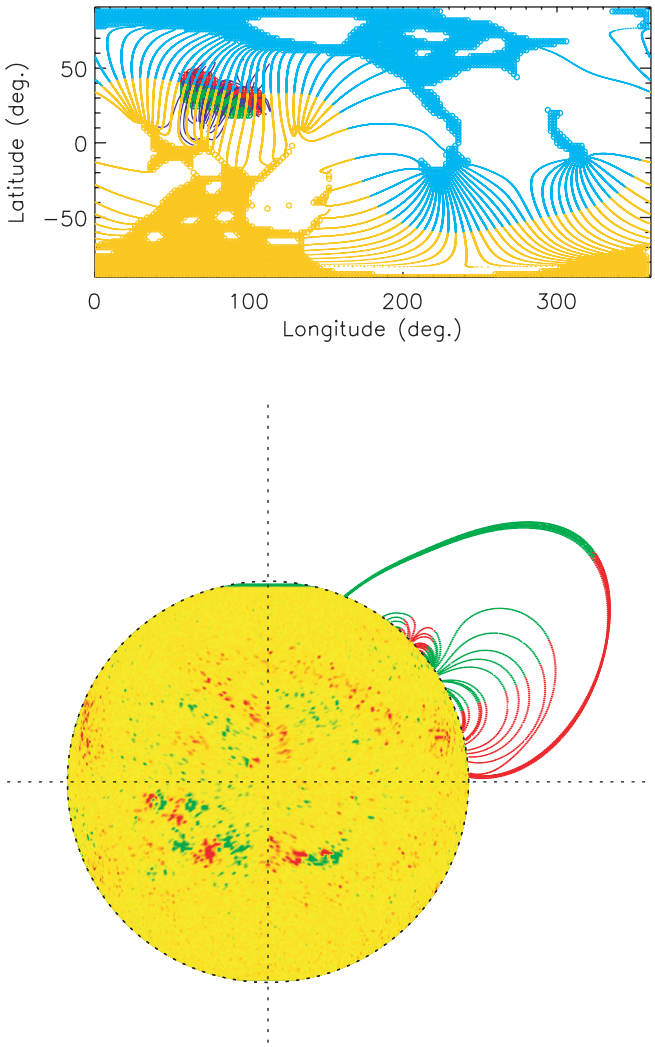

FIG. 4.—*Top*: Same as Fig. 2, but for CME on 2003 February 18. *Bottom*: Same as Fig. 2, but the projections are for field lines at longitude around 70°. This region has the antiparallel topology.

may indeed occur with a breakout topology case. But flux cancellation is not required by the breakout model but is required by the flux cancellation model. In this paper we use these terms interchangeably as appropriate in the text.

4. STATISTICS AND SOLAR CYCLE DEPENDENCE

We applied similar analyses as described in § 3 to the 80 CME events for which the source regions are located under the large-scale arcades. We found both antiparallel and parallel topologies. The statistical result is shown in Figure 5. The blue bars indicate parallel topology, and the red bars indicate antiparallel topology. It is seen that parallel topology is more common overall and in each year. On the rising phase (before year 2000) of solar cycle 23, almost all are parallel cases, but on the declining phase, there is a mixture of parallel and antiparallel cases. There are a total of 21 events with antiparallel topology and 59 events with parallel topology. The ratio between the antiparallel and parallel topology is approximately 1 : 3.

Approximate latitudes of the filament center locations are plotted on a magnetic butterfly diagram from 1995 to 2005 September in Figure 6. As described in § 3, the filament channel for each filament was identified in the MDI synoptic charts. The CR longitude and latitude of the approximate center of each filament

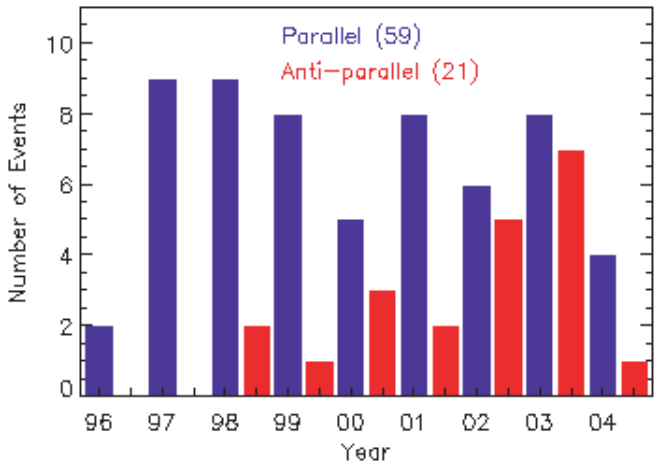

FIG. 5.—Number of events with parallel or antiparallel topology distributed by year. *Blue bars*: Parallel topology. *Red bars*: Antiparallel topology. The parallel topology is more common overall and in each year. On the rising phase (before year 2000) of solar cycle 23, almost all are parallel cases, but on the declining phase, there is a mixture of parallel and antiparallel cases. The ratio between the antiparallel (21 events) and parallel (59 events) topology is approximately 1 : 3.

channel are estimated manually using the coordinates on the charts and rounded to the nearest 5°. The 80 filaments have different sizes and shapes, so these measurements are only indicative locations, but are adequate for the purpose of overplotting on the butterfly diagram to illustrate solar cycle trends in their locations.[3] In Figure 6 the diamonds represent parallel cases and crosses the antiparallel cases. The *y*-axis is in sine latitude. The horizontal lines mark 30° latitudes north and south. Among the 80 filaments, 36 are located above 30° and 44 at or below 30°. The 36 higher latitude filaments (some are polar crown filaments) are usually in the elongated filament channels above active latitude, and the 44 lower latitude filaments are in filament channels in relatively fresh decayed active regions or between decayed active regions. There is an overall trend for the locations of this group of filaments to decrease in latitude from 1996, which is the solar minimum year, and also the beginning of our measurements, toward 2004, which is four years after solar maximum, and the end of our measurements. The trend is similar to that of the butterfly pattern but centered at higher latitudes. As discussed before, most cases on the rising phase before year 2000 are parallel cases (*diamonds*), except for only three cases. Most of the cases on the rising phase are located at or above 30°. One of the antiparallel cases is located at 30° and two just below 30°. After the solar maximum year 2000 within which the solar polar magnetic field reversed (see the color change around CR 1970 at both polar regions in the butterfly diagram in Fig. 6), there is a mixture of both

[3] The entire magnetic butterfly diagram (by David Hathway) may be found at http://science.nasa.gov/solar/dynamo.htm.

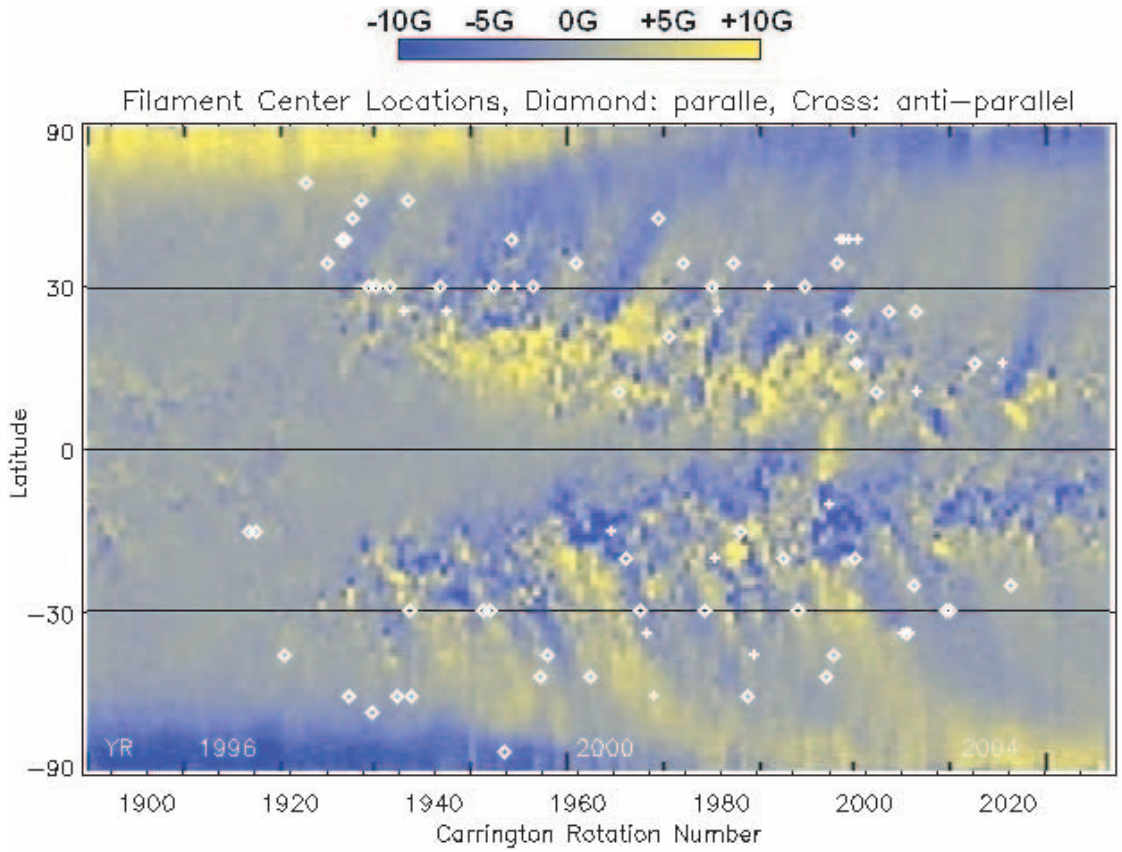

FIG. 6.—Approximate latitudes of the filament center locations are plotted on a magnetic butterfly diagram from 1995 to 2005 September (by D. Hathway). The diamonds represent parallel cases, and crosses represent antiparallel cases. The *y*-axis is in sine latitude. The horizontal lines mark 30° latitudes north and south. Among the 80 filaments, 36 are located above 30° and 44 are at or below 30°. The 36 higher latitude filaments (some are polar crown filaments) are usually in the elongated filament channels above active latitude, and the 44 lower latitude filaments are in filament channels in relatively fresh decayed active regions or between decayed active regions.

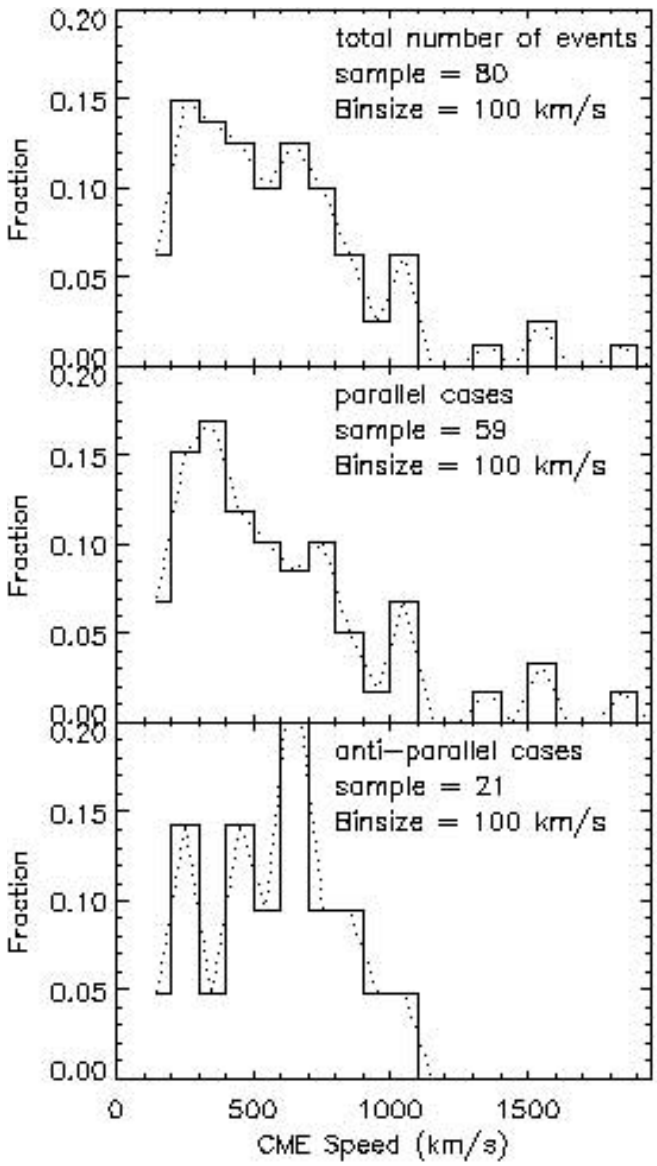

FIG. 7.—Histograms of the total 80 events (*top*), the parallel cases (*middle*), and the antiparallel cases (*bottom*). The speed ranges from 104 to 1863 km s^{-1}. Nine events (10%) have speed greater than 1000 km s^{-1}, and 42 events (50%) have speed greater than 500 km s^{-1}. The speed distributions are considerably different for CMEs with the two kinds of source region magnetic field topologies.

topologies, and no particular pattern distinguishes the locations of the two types.

We also analyzed the CME plane-of-sky linear speeds published in the same LASCO catalog[4] for a possible association between the coronal source field topology and the resulting CME speed. The CME catalog gives CME speeds from linear fits and quadratic fits, and the linear fit is preferable for 90% of CMEs (Yurchyshyn et al. 2005). The linear speeds of this group of 80 quiescent filament–related CMEs range from 104 to 1863 km s^{-1}. Figure 7 gives the distributions of the speed of all 80 events in the top panel, the parallel cases in the middle panel (ranging 104–1863 km s^{-1}), and the antiparallel cases in the bottom panel (ranging 168–1072 km s^{-1}). The overall speed peaks at low values around 300 km s^{-1}. The parallel cases (59 events) resemble the overall distribution. The antiparallel cases (21 events) have

[4] See http://cdaw.gsfc.nasa.gov/CME_list.

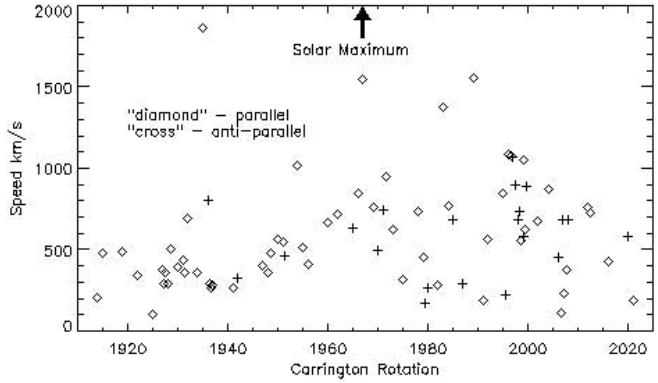

FIG. 8.—Speeds of the 80 selected CMEs presented as a function of Carrington rotations. *Diamonds*: CMEs with parallel topology. *Crosses*: CMEs with antiparallel topology. The arrow marks the solar maximum of solar cycle 23. No clear solar cycle dependence of the speeds of the 80 selected CMEs is seen.

a very different distribution and peak at a higher speed about 600 km s^{-1}, but the number of events is small. The parallel cases are responsible for the few CMEs with the highest speed at the tail of the distribution, although the speeds peak at a lower value. It is important to note that the speeds here are plane-of-sky speeds without any projection corrections, which may sometimes significantly differ from the real speed. However, in the literature the plane-of-sky speeds are used for statistical studies because it is not a straightforward matter to correct for perspective when the three-dimensional (3D) structure is unknown.

It is evident that quiescent filament–related CMEs can be as fast as nearly 2000 km s^{-1}. Of the 80 events, nine events have speeds greater than 1000 km s^{-1}, which contain over 10% of the total events, and 42 events (or over 50%) have speeds greater than 500 km s^{-1}. Quiescent filaments are not associated only with slow CMEs. On the other hand, no CME in this group has a speed over 2000 km s^{-1}. The speeds of the 80 selected CMEs are shown in Figure 8 as a function of Carrington rotation, where diamonds correspond to CMEs with parallel topology and crosses to those with antiparallel topology. Solar maximum of cycle 23 was at CR 1967, around the center of the *x*-axis. It appears that the speeds of the 80 selected CMEs do not show any clear solar cycle dependence.

5. DISCUSSIONS AND CONCLUSIONS

We have studied 80 quiescent filament–associated CME events with angular width $\geq 80^{\circ}$ that occurred during 1996–2004. This sample represents a group of wide CMEs. Using magnetogram data and a PFSS model, both parallel and antiparallel topologies are found at the CME source regions over the filament channels. We conclude that either parallel or antiparallel coronal field topologies can lead to CME initiations. It is also shown that parallel topology is more common overall and in each year. The total occurrence ratio between the antiparallel and parallel topology is about 1 : 3 with this selection of events. The parallel topology occurrence has no clear solar cycle dependence. The antiparallel topology occurrence peaks on the declining phase in the current solar cycle 23. On the rising phase of the solar cycle, there is mostly parallel topology, but on the declining phase, there is a mixture of both parallel and antiparallel topology. This result connects the occurrence of CMEs with different types of topologies over quiescent filament channels in our data set directly to the behavior of the solar magnetic cycle. During the rising phase of the cycle when the new active regions appear at their highest latitudes, their decaying field-formed filament channels tend to have polarity structures consistent with the prevailing (old cycle) polar

fields. As the solar cycle proceeds, active regions begin to emerge at lower latitudes, and around the solar maximum or the polar field reversal, more and more alternating decayed polarity bands begin to form, leading to the increased mixture of the two different coronal field topologies.

Having found that CMEs can be initiated in regions with either of the two types of magnetic topologies, other contributing factors to CME initiations for different field topologies need to be studied by means of observational data, including photospheric magnetic field variation and motion surrounding a CME, for further understanding of the initiation process. Li et al. (2004) studied the flow fields of CME source regions using a local correlation tracking (LCT) technique. They found converging flows toward the magnetic neutral lines for three cases, which may be positive evidence of flux cancellation process. Two of the CMEs are quiescent filament–related and are included in the current study. Both of these CMEs have parallel topology, where flux cancellations at the photosphere are required to enable a coronal eruption according to MHD simulations by Linker et al. (2003). Our effort on the flow fields in CME source regions with different types of field topologies is current and ongoing. Studies have been carried out in an attempt to find evidence of reconnections below and above the erupting structures using observations including EUV and SXT (Aulanier et al. 2000; Sterling & Moore 2004a, 2004b, 2005; Gary & Moore 2004; Neupert 2005; Li et al. 2005). Reconnection evidences are found at both locations, but it is difficult to distinguish which is the trigger of the eruption.

During 1996–2004, the total number of CMEs recorded in the catalog is 9239, and the number of CMEs with angular widths $\geq 80^\circ$ is 2209. Assuming about half of the events originated from the back side of the Sun, the number of front-side CMEs is about 1105. Our data set consisting of 80 events is only a small fraction of them, or about 7.24%. Thus, one should not extrapolate the results presented here to the total population of CMEs, both quiescent filament and flare-related CMEs, especially the latter. As pointed out earlier in the paper, we have not selected any active region-related CMEs for our analyses because active region fields typically have a significant departure from the potential field and may not be well described by PFSS models. We expect that the magnetic field topologies above active regions would be more complex and depend more on the local fields. We cannot extrapolate the current results to active region topologies, nor can we envision whether our results about the two kinds of topology and the solar cycle trends will hold true for CME productive active regions. Separate studies need to be carried out by different methods for active regions. Nevertheless, our study confirms that CMEs can be initiated at sites with either bipolar or quarupolar topology.

It will be interesting to find out whether MHD simulations indicate that the two types of topologies result in CMEs and ICMEs with different internal structures and energetics and hence geoeffectiveness. By iterating between the observations and modeling it should be possible to better characterize the conditions responsible for a large number of the events produced by the Sun. Li et al. (2004) studied the solar cycle dependence of the magnetic cloud polarity. Magnetic clouds are a group of special ICMEs that show clear flux-rope signatures. They found that the bipolar signatures of the magnetic clouds show a solar cycle dependence but not a simple picture. Some of our 80 CMEs are halo or partial halo CMES, which may have interplanetary CMEs (ICMEs) that encountered the Earth. In future work, we will study the corresponding ICMEs and their solar cycle dependence, and particular attention will be given to the ICME signatures related to the two different types of source region topologies.

This work is supported in part by CISM, which is funded by the NSF STC program as agreement ATM 01-20950 with Boston University, the DoD/AFOSR "Solar MURI" grant, the NSF/ATM 04-51438 award, and the NASA/SRT-NNG06GE51G award. We thank the ESA and NASA-sponsored *SOHO* project for making the MDI and EIT data accessible, and Seiji Yashiro and Nat Gopalswamy of CUA for the online CME catalog we used extensively in this study. We are grateful to NJIT Big Bear Solar Observatory for making their archive of Hα images publicly available. We also thank UCLA Mount Wilson Observatory for providing magnetic synoptic maps and C. N. Arge for generating the PFSS spherical harmonic coefficients.

APPENDIX

TABLE 1
LIST OF 80 CME EVENTS

CR	DATE	*T* (UT)	P.A. (deg)	*W* (deg)	*V* (km s^{-1})	TOPOLOGY	APPROXIMATE FILAMENT CENTER CR Long. (deg)	Lat. (deg)
1914	1996 Sep 26	05:05:05	205	103	201	P	255	−15
1915	1996 Oct 19	17:17:05	159	170	480	P	255	−15
1919	1997 Feb 07	00:30:05	Halo	360	490	P	325	−40
1922	1997 May 02	00:40:05	75	97	343	P	255	55
1925	1997 Jul 30	04:45:47	Halo	360	104	P	179	35
1927	1997 Sep 17	20:28:48	Halo	360	377	P	220	40
1927	1997 Sep 22	09:26:50	72	84	287	P	95	40
1927	1997 Sep 28	01:08:33	Halo	360	359	P	95	40
1928	1997 Oct 06	15:28:20	139	174	293	P	250	−50
1928	1997 Oct 23	11:26:50	Halo	360	503	P	80	45
1930	1997 Dec 06	10:27:05	317	223	397	P	255	50
1931	1998 Jan 02	23:28:20	Halo	360	438	P	290	30
1931	1998 Jan 21	06:37:25	Halo	360	361	P	30	−55
1932	1998 Jan 25	15:26:34	Halo	360	693	P	285	30
1934	1998 Mar 23	00:50:45	94	84	357	P	255	30
1935	1998 Apr 20	10:07:11	284	165	1863	P	350	−50
1936	1998 May 19	10:27:06	268	139	801	AP	295	25

TABLE 1—*Continued*

CR	Date	*T* (UT)	P.A. (deg)	*W* (deg)	*V* (km s^{-1})	Topology	Approximate Filament Center CR Long. (deg)	Lat. (deg)
1936	1998 May 29	13:31:10	347	86	288	P	130	50
1936	1998 Jun 09	05:55:35	253	118	265	P	20	−30
1937	1998 Jun 15	14:55:19	195	80	285	P	270	−50
1941	1998 Oct 15	10:04:36	Halo	360	262	P	80	30
1942	1998 Nov 09	18:17:55	330	190	325	AP	110	25
1947	1999 Mar 21	15:26:05	208	141	398	P	175	−30
1948	1999 Apr 17	06:36:22	213	165	362	P	185	−30
1948	1999 Apr 18	08:30:05	59	112	475	P	160	30
1950	1999 Jun 14	12:50:05	129	148	560	P	125	−70
1951	1999 Jul 07	19:31:25	303	163	547	P	205	40
1951	1999 Jul 16	20:30:05	291	131	462	AP	125	30
1954	1999 Sep 16	16:54:06	6	147	1021	P	10	30
1955	1999 Oct 25	14:26:05	186	146	511	P	185	−45
1956	1999 Nov 26	17:30:20	228	145	409	P	130	−40
1960	2000 Feb 26	23:54:05	357	104	668	P	265	35
1962	2000 May 11	23:26:06	186	141	716	P	35	−45
1965	2000 Jul 23	05:30:05	161	181	631	AP	200	−15
1966	2000 Sep 04	06:06:05	327	145	849	P	20	10
1967	2000 Sep 12	11:54:05	Halo	360	1550	P	240	−20
1969	2000 Nov 04	01:50:05	213	100	763	P	330	−30
1970	2000 Nov 26	03:30:11	259	188	495	AP	20	−35
1971	2000 Dec 25	05:06:05	219	90	741	AP	25	−50
1971	2001 Jan 14	06:30:05	327	134	945	P	75	45
1973	2001 Feb 15	13:54:05	Halo	360	625	P	325	20
1975	2001 Apr 14	23:54:05	17	133	315	P	270	35
1978	2001 Jul 12	00:06:05	240	148	736	P	275	−30
1979	2001 Aug 02	20:52:53	59	123	453	P	240	30
1979	2001 Aug 05	02:54:05	194	98	168	AP	265	−20
1980	2001 Sep 08	20:31:56	126	104	267	AP	125	25
1982	2001 Oct 28	19:27:15	333	87	279	P	240	35
1983	2001 Nov 17	05:30:06	Halo	360	1379	P	265	−15
1984	2001 Dec 20	00:30:06	113	108	769	P	270	−50
1985	2002 Feb 02	20:30:05	251	82	686	AP	60	−40
1987	2002 Mar 28	22:30:06	348	94	289	AP	50	30
1989	2002 May 22	03:50:05	Halo	360	1557	P	70	−20
1991	2002 Jun 30	04:06:06	186	92	189	P	245	−30
1992	2002 Jul 29	12:07:33	332	154	562	P	230	30
1995	2002 Oct 15	12:54:07	193	172	842	P	245	−45
1995	2002 Oct 29	20:50:05	208	104	222	AP	70	−10
1996	2002 Nov 11	15:54:05	212	93	1083	P	235	−40
1996	2002 Nov 24	20:30:05	Halo	360	1077	P	20	35
1997	2002 Dec 21	02:30:05	2	225	1072	AP	70	40
1997	2002 Dec 28	16:30:06	304	84	901	AP	70	40
1998	2003 Jan 03	18:06:05	274	127	682	AP	340	25
1998	2003 Jan 20	18:30:05	315	105	733	AP	65	40
1998	2003 Jan 20	21:30:05	58	166	555	P	340	20
1999	2003 Jan 27	22:23:27	205	267	1053	P	325	−20
1999	2003 Jan 29	05:06:05	343	96	582	AP	310	15
1999	2003 Jan 30	10:06:05	2	138	620	P	260	15
1999	2003 Feb 18	02:42:06	312	93	888	AP	70	40
2002	2003 Apr 26	21:50:05	48	166	672	P	160	10
2004	2003 Jun 14	01:54:05	26	195	875	P	325	25
2006	2003 Aug 07	20:30:05	177	80	449	AP	300	−35
2006	2003 Aug 17	17:54:05	139	201	111	P	150	−35
2007	2003 Sep 07	16:54:05	245	116	685	AP	265	−35
2007	2003 Sep 07	21:54:05	223	91	227	P	295	−25
2007	2003 Sep 14	21:30:08	232	88	377	P	165	25
2008	2003 Oct 05	30:05:05	267	86	684	AP	20	10
2012	2004 Jan 21	04:54:05	Halo	360	762	P	220	−30
2012	2004 Jan 21	12:30:05	129	111	727	P	220	−30
2016	2004 May 24	21:26:08	354	131	426	P	55	15
2020	2004 Sep 05	06:54:06	310	87	580	AP	175	15
2021	2004 Oct 07	19:30:05	210	87	189	P	60	−25

Note.—CR: Carrington rotation. P.A.: Position angle. *W*: Angular width. *V*: Plane of sky speed. P: Parallel. AP: Antiparallel.

REFERENCES

Aly, J. J. 1991, ApJ, 375, L61
Amari, T., Luciani, J. F., Aly, J. J., Mikic, Z., & Linker, J. 2003a, ApJ, 585, 1073
———. 2003b, ApJ, 595, 1231
Antiochos, S. K. 1998, ApJ, 502, L181
Antiochos, S. K., DeVore, C. R., & Klimchuk, J. A. 1999, ApJ, 510, 485
Aulanier, G., DeLuca, E. E., Antiochos, S. K., McMullen, R. A. & Golub, L. 2000, ApJ, 540, 1126
Bothmer, V., & Schwenn, R. 1994, Space Sci. Rev., 70, 215
Cliver, E. W., St. Cyr, O. C., Howard, R. A., & McIntosh, P. S. 1994, in IAU Colloq. 144, Solar Coronal Structures, ed. V. Rusin et al. (Tatranská Lomnica: VEDA), 83
Cremades, H., & Bothmer, V. 2004, A&A, 422, 307
DeVore, C. R., & Antiochos, S. K. 2005, ApJ, 628, 1031
Forbes, T. 2000, J. Geophys. Res., 105, 23153
Gary, G. A., & Moore, R. L. 2004, ApJ, 611, 545
Gibson, S. E., & Fan, Y. 2006, ApJ, 637, L65
Gibson, S. E., Fan, Y., Mandrini, C., Fisher, G., & Demoulin, P. 2004, ApJ, 617, 600
Gilbert, H. R., Holzer, T. E., Burkepile, J. T., & Hundhausen, A. J. 2000, ApJ, 537, 503
Gopalswamy, N., Lara, A., Yashiro, S., & Howard, R. A. 2003a, ApJ, 598, L63
Gopalswamy, N., Shimojo, M., Lu, W., Yashiro, S., Shibasaki, K., & Howard, R. A. 2003b, ApJ, 586, 562
Gosling, J. T. 1993, J. Geophys. Res., 98, 18937
Gosling, J. T., McComas, D. J., Phillips, J. L., & Bame, S. J. 1991, J. Geophys. Res., 96, 7831
Howard, R. A., Sheeley, N. R. Jr., Koomen, M. J., & Michels, D. J. 1985, J. Geophys. Res., 90, 8137
Jing, J., Yurchyshyn, V. B., Yang, G., Xu, Y., & Wang, H. 2004, ApJ, 614, 1054
Li, J., Mickey, D. L., & LaBonte, B. J. 2005, ApJ, 620, 1092
Li, Y., & Luhmann, J. G. 2004, J. Geophys. Res., 66, 323
Li, Y., Luhmann, J. G., Fisher, G. F., & Welsch, B. T. 2004, J. Atmos. Solar Terr. Phys., 66, 1271
Li, Y., Luhmann, J. G., Mulligan, T., Hoeksema, J. T., Arge, C. N., Plunkett, S. P., & Cyr, O. C. St. 2001, J. Geophys. Res., 106, 25103
Linker, J. A., Lionello, R., Mikic, Z., & Amari, T. 2001, J. Geophys. Res., 106, 25165
Linker, J. A., & Mikic, Z. 1995, ApJ, 438, L45
Linker, J. A., Mikic, Z., Lionello, R., Riley, P., Amari, T., & Odstrcil, D. 2003, Phys. Plasmas, 10, 1971
Low, B. C. 1996, Sol. Phys., 167, 217
Luhmann, J. G., Gosling, J. T., Hoeksema, J. T., & Zhao, X. 1998, J. Geophys. Res., 103, 6585
Lynch, B. J., Antiochos, MacNeice, P. J., Zurbuchen, T. H., & Fisk, L. A. 2004, ApJ, 617, 589
McComas, D. J., Gosling, J. T., Hammond, C. M., Moldwin, M. B., Phillips, J. L., & Forsyth, R. J. 1995, Space Sci. Rev., 72, 129
Moore, R. L., & Sterling, A. C. 2006, in AGU Monograph: Solar Eruptions and Energetic Particles, ed. N. Gopalswamy, R. Mewaldt, & J. Torsti (Washington: Am. Geophys. Union), in press
Neupert, W. M. 2005, Hvar Obs. Bull., 29, 187
St. Cyr, O. C., et al. 2000, 105, 18169
Sterling, A. C., & Moore, R. L. 2004a, ApJ, 602, 1024
———. 2004b, ApJ, 613, 1221
———. 2005, ApJ, 630, 1148
Sturrock, P. 1991, ApJ, 380, 655
Vourlidas, A., Subramanian, P., Dere, K. P., & Howard, R. A. 2000, ApJ, 534, 456
Webb, D. F. 1995, Rev. Geophys., 33, 577
———. 1998, in IAU Colloq. 167, New Perspectives on Solar Prominences, ed. D. F. Webb et al. (ASP Conf. Ser. 150; San Francisco: ASP), 463
———. 2000, J. Atmos. Solar Terr. Phys., 62, 1415
Yashiro, S., Gopalswamy, N., Michalek, G., St. Cyr, O. C., Plunkett, S. P., Rich, N. B., & Howard, R. A. 2004, J. Geophys. Res., 109, A07105
Yurchyshyn, V., Yashiro, S., Abramenko, V., Wang, H., & Gopalswamy, N. 2005, ApJ, 619, 599
Zhang, J., Dere, K. P., Howard, R. A., Kundu, M. R., & White, S. M. 2001, ApJ, 559, 452